Exploring the $Pb_{1-x}Sr_xHfO_3$ System and Potential for High Capacitive Energy Storage Density and Efficiency

Megha Acharya[1,2], Ella Banyas[2], Maya Ramesh[1], Yizhe Jiang[1], Abel Fernandez[1], Arvind Dasgupta[1], Handong Ling[1], Brendan Hanrahan,[3] Kristin Persson[1,2,4], Jeffrey B. Neaton[2,4,5,6], Lane W. Martin[1,2*]

[1] Department of Materials Science and Engineering, University of California, Berkeley, Berkeley, CA 94720, USA

[2] Materials Sciences Division, Lawrence Berkeley National Laboratory, Berkeley, CA 94720, USA

[3] U.S. Army Research Laboratory, Adelphi, MD 20783, USA

[4] Molecular Foundry, Lawrence Berkeley National Laboratory, Berkeley, CA 94720, USA

[5] Department of Physics, University of California, Berkeley, Berkeley, CA 94720, USA

[6] Kavli Energy Nanosciences Institute, University of California, Berkeley, CA 94720, USA

*lwmartin@berkeley.edu

Keywords: Antiferroelectric, energy-storage, pulsed-laser deposition, dielectric, hafnate

Abstract

The hafnate perovskites $PbHfO_3$ (antiferroelectric) and $SrHfO_3$ ('potential' ferroelectric) are studied as epitaxial thin-film heterostructures on $SrTiO_3$ (001) substrates with the added opportunity of observing a morphotropic phase boundary in the $Pb_{1-x}Sr_xHfO_3$ system akin to that in $PbZr_xTi_{1-x}O_3$. The resulting (240)-oriented $PbHfO_3$ (*Pba*2) films were found to exhibit antiferroelectric switching with a saturation polarization ~53 $\mu C/cm^2$ at 1.6 MV/cm and a weak-field dielectric constant ≈186 at 298 K. Temperature-dependent dielectric

This article has been accepted for publication and undergone full peer review but has not been through the copyediting, typesetting, pagination and proofreading process, which may lead to differences between this version and the Version of Record. Please cite this article as doi: 10.1002/adma.202105967.

measurements revealed an antiferroelectric-to-paraelectric phase transition at ~518 K. Further, (002)-oriented $SrHfO_3$ films were synthesized, but were found to not exhibit ferroelectric behavior; nor did we observe evidence of a recently reported polar *P*4*mm* phase. Instead, the $SrHfO_3$ films were found to exhibit a weak-field dielectric constant ≈25 at 298 K and no signs of a structural transition to a polar phase as a function of temperature (77-623 K) and electric field (-3 MV/cm to 3 MV/cm). While the lack of ferroelectric order in $SrHfO_3$ removed the potential for a $PbZr_xTi_{1-x}O_3$-like morphotropic phase boundary, we proceeded to explore the structural and property evolution of the $Pb_{1-x}Sr_xHfO_3$ ($0 \leq x < 1$) system. Strontium alloying was found to increase the electric-breakdown strength (E_B) and decrease the hysteresis loss resulting in concurrent enhancement of the capacitive energy storage density (U_r) and efficiency (η). An optimum composition ($Pb_{0.5}Sr_{0.5}HfO_3$) was found to produce the best combination of $E_B = 5.12 \pm 0.5$ MV/cm, $U_r = 77 \pm 5$ J/cm^3, and $\eta = 97 \pm 2\%$; well out-performing $PbHfO_3$ and other antiferroelectric oxides.

Introduction

Hafnate-based thin films, in both perovskite[1,2] and non-perovskite[3,4] phases, have garnered extensive attention owing to their potential applications as gate materials and/or ferroelectric memories in complementary metal-oxide-semiconductor (CMOS) devices. Additionally, many antiferroelectric hafnate systems[5-8] have been found to be promising for capacitive energy storage applications as compared to their ferroelectric and dielectric counterparts[9-11]. Among the range of materials that could be studied, two potentially exciting hafnate perovskite oxides are $PbHfO_3$ and $SrHfO_3$. $PbHfO_3$ (*Pba*2, lattice parameters: $a = 5.854$ Å, b

= 11.694 Å, c = 8.191 Å[12]) has been synthesized and its structural[13,14], optical[15] and dielectric[16] properties have been probed in bulk ceramics and single crystals. It exhibits a switching-field-induced phase transition from an antiferroelectric *Pbam* to a ferroelectric *Pba*2 phase at ~250 kV/cm, characterized by a double polarization-hysteresis loop. $PbHfO_3$ is isostructural to the archetypal antiferroelectric $PbZrO_3$ (*Pba*2, lattice parameters: a = 5.88 Å, b = 11.77 Å, c = 8.22 Å[17]), has a large band gap (3.4 eV[18]), and a dielectric constant ≈90 at room temperature[12]. There have been a few reports wherein $PbHfO_3$ has been produced as polycrystalline thin films including those produced by atomic-layer deposition[19-21] and exploring the antiferroelectric, electrocaloric, and energy-storage properties.

$SrHfO_3$ has also been synthesized using solid-state reaction methods and its structural properties have been examined[22]. In the bulk, $SrHfO_3$ exhibits a *Pnma* structure at ambient conditions. Other polymorphs (*i.e.*, *Cmcm*, *I*4*/mcm*, $Pm\bar{3}m$) are observed upon heating-induced structural-phase transitions by virtue of changes in the HfO_6 octahedral-tilt angles. Studies of the dielectric[23] and optical[24] properties revealed low dielectric constant (17-25[25]) and large band gap (6.1 eV[22]). While there has been speculation about the appearance of temperature-induced soft-phonon modes in the *Cmcm* and *I*4*/mcm* phases, these were found to be associated with octahedral rotations. Similarly, the dominant lattice instabilities in the $Pm\bar{3}m$ phase have also been shown in experimental and theoretical studies to be antiferrodistortive modes, leading to non-polar phases that do not give rise to ferroelectric behavior[23,26]. This said, a recent report focused on epitaxial thin films[27] suggested a tetragonal *P*4*mm* structure can be produced which gives rise to a piezoelectric response (ε_{33}= 8.8 C/m^2) and further suggests that this phase could be ferroelectric. Despite these

interesting observations there is little work, especially on thin films of both systems, and the true nature of properties of these potentially interesting materials as thin films could stand to be better understood.

While additional studies of thin films of the parent compounds are warranted, an intriguing possibility is also presented as it relates to solid solutions of these materials (*i.e.*, $Pb_{1-x}Sr_xHfO_3$). First, the combination of the antiferroelectric *Pbam* $PbHfO_3$ and (potentially) ferroelectric *P*4*mm* $SrHfO_3$[27] could give rise to a morphotropic phase boundary (MPB), analogous to that in the well-studied $PbZr_xTi_{1-x}O_3$ (PZT) system. Recent *ab initio* predictions have shown that even apart from a prospective structural-phase boundary, $Pb_{1-x}Sr_xHfO_3$ could exhibit enhanced piezoresponse as a function of ionic disorder (with strontium alloying)[28]. Finally, strontium alloying is well known to improve the leakage and breakdown strength of lead-based perovskites[29] and thus there is potential that the $Pb_{1-x}Sr_xHfO_3$ system could provide a pathway to improved capacitive energy storage performance. The key parameters underlying capacitive-energy storage of any dielectric material are the recoverable energy density in the charge-discharge process ($U_r = \int_{P_r}^{P_{max}} EdP$, where P_r and P_{max} are the remanent and maximum polarization, respectively) and the energy-storage loss (U_{loss}, which is determined by the area enclosed within the double hysteresis loops). U_r and U_{loss} dictate the overall efficiency in the charge-discharge process [$\eta = (U_r/(U_r+U_{loss}))$][30]. Multiple design strategies have been adopted in order to enhance the U_r and η values in antiferroelectric materials with chemical alloying[31-33] being a common choice and it is possible that in $Pb_{1-x}Sr_xHfO_3$ such an approach could be effective due to reduced leakage,

improved breakdown strength, and increased polarization in the parent antiferroelectric $PbHfO_3$.

Here, we synthesize epitaxial $Pb_{1-x}Sr_xHfO_3$ (x = 0, 0.05, 0.15, 0.25, 0.5, 0.75, 1) thin films across a range of temperatures, oxygen partial pressures, substrates, laser fluences, etc. to explore this system. The results are organized into three sections. The first, focuses on $PbHfO_3$ thin films wherein (240_O)-oriented (*Pbam*; the subscript "O" represents lattice indexing for the orthorhombic structure) films which exhibit robust antiferroelectric behavior and undergo an electric-field-induced phase transition to a ferroelectric phase (*Pba*2). The measured polarization was 53 μC/cm^2 at 1.6 MV/cm with a weak-field dielectric constant ≈186 at 298 K and a dielectric anomaly centered at ~518 K, characteristic of the antiferroelectric-to-paraelectric phase transition. The second section focuses on $SrHfO_3$ thin films wherein (002)-oriented ($Pm\bar{3}m$) films were produced. Despite extensive study, no evidence of polar order was observed as a function of temperature and/or applied electric fields. The measured polarization was 0.3 μC/cm^2 at 3 MV/cm with a weak-field dielectric constant ≈25 at 298 K. Finally, the last section focuses on 75-nm-thick (240_O)-oriented $Pb_{1-x}Sr_xHfO_3$ ($0 < x < 1$) films. While the absence of polar, ferroelectric behavior in the $SrHfO_3$ films meant that MPB phenomena akin to those in the PZT system is improbable, strong impact on the evolution of the polarization-electric field response (and therefore capacitive-energy-storage properties) were found. Increasing strontium content enhances the electric-breakdown strength (E_B) and decreases U_{loss}, both of which play a critical role in increasing the U_r and η values. $Pb_{0.5}Sr_{0.5}HfO_3$ was found to exhibit the highest E_B (5.12 MV/cm; three-times the value of 1.23 MV/cm for $PbHfO_3$), a 6% increase in the η values (from 91% for

$PbHfO_3$ to 97%), a 2.7-times increase in U_r (from 21 J/cm^3 for $PbHfO_3$ to 77 J/cm^3), and a 10^6-times improvement in fatigue endurance at E_B = 1.23 MV/cm. This performance places $Pb_{0.5}Sr_{0.5}HfO_3$ among the most promising antiferroelectrics for such applications.

Results and Discussion

$PbHfO_3$

Motivated by the multiple studies probing the energy-storage properties of antiferroelectric oxides due to their unique property of undergoing an antiferroelectric-to-ferroelectric phase transition upon application of electric field[29,33,34], we synthesized and characterized single-crystalline antiferroelectric $PbHfO_3$ films. In the current work, 15-360-nm-thick (240_O)-oriented $PbHfO_3$ (**Figure 1**a) films were deposited on a range of substrates at a range of growth conditions using pulsed-laser deposition (Experimental Section). For brevity, X-ray diffraction scans have been included for 75-nm-thick films grown at a fixed heater temperature (650°C), laser fluence (1.7 J/cm^2), and variable dynamic oxygen-partial pressure (10-100 mTorr) using 45-55-nm-thick $SrRuO_3$ layers as the top and bottom electrodes (Figure 1b). Rutherford backscattering spectrometry (Experimental Section) was used to probe the film stoichiometry. The growth pressure can be used to control the Pb:Hf ratio in the $PbHfO_3$ heterostructures (Figure S1, Supporting Information) whereby decreasing the oxygen-partial pressure during growth from 100 mTorr to 10 mTorr (at a fixed laser fluence and heater temperature of 1.1 J/cm^2 and 600°C, respectively) results in a decrease in the Pb:Hf ratio (*i.e.,* decrease in the percentage of the heavier cation, Pb^{2+}) in the films with optimized chemistry

found for growth at ~30 mTorr. Such trends are similar to those observed in other perovskite oxides[35].

The epitaxy of the $PbHfO_3$ films was determined using off-axis azimuthal (ϕ) scans (Experimental Section). Scans were completed about the $SrTiO_3$ (substrate) 103- and $PbHfO_3$ (film) 362_O-diffraction conditions, wherein the substrate is expected and observed to have four peaks (Figure 1c) and the *Pbam* phase of $PbHfO_3$ is expected to exhibit two peaks (*i.e.*, 362_O and $36\bar{2}_O$) separated by ϕ =180°. The scan (Figure 1d), however, revealed the presence of four peaks for the $PbHfO_3$ which is consistent with the presence of two rotational structural variants (labeled I and II; Figure S2, Supporting Information), rotated by 90° with respect to each other (such that they align with the peaks for the $SrTiO_3$ substrate). Thus, the epitaxy is found to be $PbHfO_3$ $[001_O]$ || $SrTiO_3$ [010] for rotational variant I and $PbHfO_3$ $[001_O]$ || $SrTiO_3$ [100] for rotational variant II with $PbHfO_3$ $[240_O]$ || $SrTiO_3$ [001] for both cases. The lattice parameters were determined to be a_O = 5.88 ± 0.005 Å, b_O = 11.63 ± 0.005 Å, and c_O = 8.30 ± 0.005 Å (consistent with an orthorhombic crystal structure) using reciprocal space mapping (RSM) studies about the 084_O- and 362_O-diffraction conditions of the $PbHfO_3$ (Figure S3, Supporting Information).

Having determined the crystal structure and chemical composition of the epitaxial films, the electrical properties of the $PbHfO_3$ heterostructures were also probed. In the bulk, $PbHfO_3$ has been reported to undergo two structural phase transitions. The first is to another antiferroelectric phase (the crystal structure and space-group symmetry of which has not yet been established) at 436 K which is unlikely to be resolved in dielectric measurements for thin films[20]. The second is a transition to the paraelectric cubic phase ($Pm\bar{3}m$) reported to be

in the temperature range of 476-484 K[16,36,37,38]. The dielectric constant and loss as a function of temperature for the films produced herein display evidence of a phase transition from the antiferroelectric (*Pba*2) to the paraelectric ($Pm\bar{3}m$) phase at ~518 K (Figure 1e). All the synthesized heterostructures exhibited a double-hysteresis loop in their polarization response indicative of antiferroelectric behavior[39]. The relatively high leakage current density in the $PbHfO_3$ films grown at high pressures (100 mTorr), however, was found to prevent the measurement of fully saturated double-hysteresis loops (Figure S4, Supporting Information). Apart from modifying the Pb:Hf ratio in the synthesized thin films, changes in the growth pressure played a critical role in our ability to observe the antiferroelectric properties of the $PbHfO_3$ heterostructures. Decreasing the growth pressure is expected to introduce a multitude of structural point defects as well as defect clusters due to the knock-on damage induced by the enhanced kinetic energy of the incident adatoms. The presence of such defects in ferroelectric $PbTiO_3$ has been shown to produce deep-trap states (which cannot be readily activated) associated with defect complexes resulting in enhanced resistivity[40,41]. The defect clusters can be composed of cation and/or anion vacancies, and potential interstitials or antisites[42]. Using the same hypothesis, we observed an increase in the maximum electric field that can be applied to the $PbHfO_3$ heterostructures from 1 MV/cm (100 mTorr) to 1.23 MV/cm (10 mTorr; Figure 1f and Figure S4, Supporting Information) with substantial reduction in the leakage current density. The ability to obtain fully saturated and slim double-hysteresis loops in the polarization response helped in determining the true energy-storage parameters of the $PbHfO_3$ films. Additionally, substitution of lead with strontium is expected to affect the polar ordering and enhance the stability of the antiferroelectric state[29]. There are

no reports, however, demonstrating the same for $PbHfO_3$ heterostructures, making a systematic study of strontium alloying especially worthwhile.

$SrHfO_3$

$SrHfO_3$ has been synthesized and studied in various polymorphic forms (**Figure 2**a,b and Figure S5, Supporting Information). The presence of a metastable polar, piezoelectric $SrHfO_3$ (*P*4*mm*) phase has recently been reported[27]. To investigate the structure and properties of $SrHfO_3$ thin films, we synthesized highly crystalline $(001)_{pc}$-oriented $SrHfO_3$ (subscript "pc" represents pseudocubic) on $SrTiO_3$ (001) (a = 3.905 Å) and other substrates (Experimental Section) as confirmed by X-ray diffraction measurements (Figure 2c). Further, RSM studies (Figure S6, Supporting Information) performed about the $SrHfO_3$ 103_{pc}- and 101_{pc}-diffraction conditions were used to extract the lattice parameters as a_{pc} = 4.08 ± 0.005 Å, b_{pc} = 4.07 ± 0.005 Å, and c_{pc} = 4.08 ± 0.005 Å. The extracted c/a = 1.0004 (~1) accompanied with the reports about synthesis of a cubic crystal symmetry of $SrHfO_3$ as thin films in the literature[2,24,49,50] suggests that the crystal structure of the as-grown $SrHfO_3$ phase is likely to be a cubic ($Pm\bar{3}m$) symmetry as well. High-quality crystalline $SrHfO_3$ thin films (with cubic $Pm\bar{3}m$ symmetry) were obtained on $NdScO_3$ (110) substrates as well. We do note the formation of a minority secondary phase – likely the thermodynamically stable $SrHfO_3$ (*Pnma*) phase – for some combinations of total laser pulses (or the film thickness), partial pressure of oxygen, and temperature (Figure S7, Supporting Information). Off-axis azimuthal (ϕ) scans about the 103-diffraction condition for both the substrate (Figure 2d) and film

(Figure 2e) revealed the epitaxy to be $SrHfO_3$ [100] || $SrTiO_3$ [100], $SrHfO_3$ [010] || $SrTiO_3$ [010], and $SrHfO_3$ [001] || $SrTiO_3$ [001].

We proceeded to perform electrical characterization to search for evidence of a structural phase transition (commensurate with a dielectric anomaly) to the *P*4*mm* phase. The dielectric constant and loss (Figure 2f and Figure S8, Supporting Information) were measured as a function of temperature (77-623 K) and reveal a weak-field dielectric constant ≈25 at room temperature and no evidence of an anomaly across the temperature range probed herein. Such behavior has been seen in $CdTiO_3$[43] which undergoes a structural phase transition below room temperature (77 K) from a non-polar (*Pnma*) to polar ($Pna2_1$) phase. Polarization-electric field measurements (from -3 MV/cm to 3 MV/cm) were completed as a function of temperature (77-623 K) and reveal low polarization response (~0.3 μC/cm^2 at maximum field) for 33-400-nm-thick $SrHfO_3$ heterostructures grown on $SrRuO_3$-buffered $SrTiO_3$ (001) (Figure 2g). Again, there was an absence of non-linearity or hysteresis in the polarization response across the entire temperature range studied. Taken together, this suggests that the $SrHfO_3$ films produced here are not ferroelectric across the temperature range (77-623 K) nor under applied electric field (-3 MV/cm to 3 MV/cm).

The observation of the cubic ($Pm\bar{3}m$) $SrHfO_3$ phase and the absence of ferroelectric behavior led us to examine this material in more detail, akin to prior studies[44]. Although, prior first-principles density functional theory (DFT) calculations of the phonon spectra of the bulk $SrHfO_3$ ($Pm\bar{3}m$) phase reported the presence of zone-center polar instabilities; the same calculations show that the dominant phonon instabilities are antiferrodistortive zone-boundary modes. This result is consistent with the observed low-temperature, non-polar

ground state (*i.e.*, the *Pnma* phase)[45,46]. While the stabilization of the cubic crystal symmetry in thin films indicates a suppression of the antiferrodistortive modes, the absence of a *P*4*mm* phase further suggests that the ferroelectric instability was likewise suppressed. Using DFT within the local density approximation (LDA), we examined the energy landscape across the structural distortion from the non-polar to the polar phase[47] (Experimental Section). A small monotonic decrease in energy was computed along a polar distortion path (0.62 meV/atom for DFT-LDA; Figure S9a, Supporting Information). When compared to the DFT-LDA calculations of the energy differences between the $Pm\bar{3}m$ and *P*4*mm* structures in the known ferroelectrics[48] [*e.g.*, $PbTiO_3$ (ΔE = 11.6 meV/atom) and $BaTiO_3$ (ΔE = 1.0 meV/atom)], the smaller energy difference for $SrHfO_3$, combined with the presence of zone-boundary instabilities, are consistent with the lack of appearance of the *P*4*mm* phase in the synthesized films. Similar results were obtained for DFT-PBE calculations as well (Figure S9b, Supporting Information). In summary, the DFT calculations performed here along with prior ones in the literature are consistent with the absence of any significant polar distortion or hysteresis in the polarization response of the as-grown $SrHfO_3$ films. Additionally, prior work for bulk $SrHfO_3$, corroborates the fact that we did not find any evidence of a tetragonal (*P*4*mm*) structure despite extensive electrical studies across a wide temperature range[23,22,49]. Other experimental studies of $SrHfO_3$ thin films, including those looking at its growth on semiconductor substrates such as Si (001) and Ge (001)[24,46,50] also report a suppression of all instabilities, similar cubic structures, and relatively low dielectric constant (~30). Additionally, Raman spectroscopy investigating the temperature-induced soft-phonon modes in the $SrHfO_3$ polymorphs suggest the possibility of modes that would give rise to

antiferrodistortive character rather than ferrodistortive character[23]. Consistent with these works, at least for the explored growth conditions here, the stable phase of $SrHfO_3$ in the synthesized thin films is found to be cubic and non-polar.

With the absence of ferroelectric behavior in the $SrHfO_3$ films, the possibility of a structural phase-boundary akin to the MPB in PZT across the $PbHfO_3$-$SrHfO_3$ solid solution seemed unlikely. We did, however, observe antiferroelectric switching behavior and low dielectric loss in the synthesized $PbHfO_3$ thin films, necessitating further studies in the same and the exploration of the $Pb_{1-x}Sr_xHfO_3$ system as a pathway to further improve performance. Especially with the slightly smaller ionic radius of Sr^{2+} cations, the tolerance factor of the solid solutions is expected to be lower than $PbZrO_3$, resulting in an increased Curie temperature and a more stable antiferroelectric phase with a lower dielectric constant and hysteresis loss[29]. Prior studies of the $Pb_{1-x}Sr_xZrO_3$ system also do not explore the entire phase diagram (*i.e.*, beyond x = 0.05). Though not useful as a ferroelectric, $SrHfO_3$ is likely to improve the antiferroelectric and energy-storage properties of $PbHfO_3$ when synthesized as a solid solution.

$PbHfO_3$-$SrHfO_3$ solid solutions

With the desire to alter the properties of $PbHfO_3$, we proceeded to explore the synthesis and energy-storage properties of $Pb_{1-x}Sr_xHfO_3$ thin films. We synthesized and characterized epitaxial $Pb_{1-x}Sr_xHfO_3$ (x = 0.05, 0.15, 0.25, 0.5, 0.75) thin films using similar conditions and approaches (Experimental Section). With the difference between the ionic radii of Pb^{2+} (149 pm) and Sr^{2+} (144 pm) ions being small (3% difference), isovalent substitution is expected to

be feasible while forming a stable single-phase solid solution. Following synthesis of the $Pb_{1-x}Sr_xHfO_3$ compounds, X-ray diffraction studies were completed to probe the evolution of the crystal structure. Highly crystalline, single-phase, solid-solution films were obtained for all compositions explored (Figure 3). The crystallinity of the synthesized films with respect to the substrate was ascertained using rocking curves and azimuthal (ϕ) scans (Figures S10 and S11, Supporting Information). The $Pb_{1-x}Sr_xHfO_3$ ($0 < x < 1$) 240_O-diffraction peaks, in all cases, appear to shift (minimally) to higher θ-2θ values (*i.e.*, corresponding a reduction of the out-of-plane lattice parameter) with increasing strontium content. This is expected due to the isovalent substitution of a (slightly) smaller-sized Sr^{2+} cation at the Pb^{2+} site. Additional RSM studies were performed about the 362_O- and 084_O-diffraction conditions of $PbHfO_3$ and the 103-diffraction condition of the $SrTiO_3$ (001) substrate (Figure S12a-j, Supporting Information) to obtain the lattice parameters (with an error bar of ±0.005 Å) of all the compositions. The overall change in all the three lattice parameters (*a*, *b*, and *c*) with respect to that of the parent $PbHfO_3$ was found to be minimal. Again, this can be rationalized from the fact that there is only a small difference (3%) in the ionic radii of the Sr^{2+} and Pb^{2+} cations (Figure S12k-l, Supporting Information).

Although all the $Pb_{1-x}Sr_xHfO_3$ compositions appear isostructural, they exhibited a varied range of electrical properties. Frequency-dependent studies of the dielectric constant (**Figure 4**a) reveal that increasing strontium content results in a reduction in the dielectric constant from ≈186 for x = 0 to ≈25 for x = 1 (the loss remains low for all compositions; Figure S13, Supporting Information). Likewise, the AC-field-dependent evolution of the dielectric constant (Figure 4b) for all $Pb_{1-x}Sr_xHfO_3$ compositions was examined. A typical

ferroelectric material is expected to display a peak in the dielectric response upon increasing the AC electric field due to the increase in the ferroelectric domain-wall contribution to the dielectric constant [51]. Antiferroelectric materials are expected to exhibit a similar behavior, but at a relatively higher applied AC electric field (*i.e.*, at values corresponding to the antiferroelectric-to-ferroelectric phase transition, E_F)[52,53]. Below E_F, however, antiferroelectric $PbZrO_3$ thin films have been found to exhibit a weak residual ferroelectric phase[54] due to unbalanced antiparallel shift of oxygen atoms along the [001]. A similar AC field-dependent dielectric response with a peak at ~23 kV/cm was observed for $PbHfO_3$ which can be considered as an additional attribute associated with its antiferroelectric nature. The peak in dielectric response, however, was found to diminish in $Pb_{1-x}Sr_xHfO_3$ solid solutions with increasing strontium content, until the system ultimately exhibits a fixed dielectric constant value with increasing applied AC electric field. This indicates diminishing antiferroelectric behavior in $Pb_{1-x}Sr_xHfO_3$ ($x > 0$) compositions as compared to $PbHfO_3$. Further, the absence of peaks in the switching current hysteresis loops (as compared to $PbHfO_3$) also reinforces the idea of a reduction in or absence of the antiferroelectric state in $Pb_{1-x}Sr_xHfO_3$ ($x > 0$)[54].

We also probed the effect of strontium substitution on the E_B by measuring the polarization response as a function of electric field for 15 capacitors for the various $Pb_{1-x}Sr_xHfO_3$ films up to their electrical breakdown and used the Weibull-distribution function (Experimental Section) to extract a statistically meaningful breakdown field for each material (Figure 4c and Figure S14, Supporting Information)[55]. The highest $E_B = 5.12 \pm 0.5$ MV/cm was observed for $Pb_{0.5}Sr_{0.5}HfO_3$ which is three-times the value obtained for $PbHfO_3$ (1.23

MV/cm). Multiple parameters can affect the E_B of a dielectric capacitor, including the dielectric constant, leakage current density (Figure S15), electronic bandgap, microstructure, sample thickness, defect chemistry, electrode configuration, *etc.*[56] Considering that the growth parameters, sample geometry and thickness, and electrode configuration for the various $Pb_{1-x}Sr_xHfO_3$ heterostructures are identical, the variables most likely to alter the E_B of the different $Pb_{1-x}Sr_xHfO_3$ ($0 < x < 1$) compositions are likely the bandgap and dielectric constant. The experimentally reported optical band-gap values for $PbHfO_3$ and $SrHfO_3$ are 3.4 eV[18] and 6.1 eV[24], respectively. Thus, strontium substitution could potentially improve the E_B performance by either (or both) increasing the bandgap and/or decreasing the dielectric constant. Additionally, there can be changes to the leakage current density (*i.e.*, the higher the leakage current density, the lower the E_B) with strontium substitution which can contribute to altering the E_B. While we can confirm the effect of strontium on the dielectric permittivity and leakage current density, additional optical studies are required to explore the bandgap aspect. Next, the polarization response was measured for all the compositions driven up to their corresponding E_B values [*i.e.*, $PbHfO_3$ (±1.23 MV/cm), $Pb_{0.95}Sr_{0.05}HfO_3$ (±3.52 MV/cm), $Pb_{0.85}Sr_{0.15}HfO_3$ (±3.52 MV/cm), $Pb_{0.75}Sr_{0.25}HfO_3$ (±3.94 MV/cm), $Pb_{0.5}Sr_{0.5}HfO_3$ (±5.12 MV/cm), and $Pb_{0.25}Sr_{0.75}HfO_3$ (±2.31 MV/cm)] at 10 kHz (Figure 4d). The saturation polarization for all the compositions was found to vary from 0.3-44 $\mu C/cm^2$ depending on the extent of strontium substitution (x) (*i.e.,* a smaller value of polarization was observed at a given applied electric field with increasing strontium content).

Using these data, we can also explore the evolution of capacitive-energy-storage performance. The values for U_r and the overall efficiency η were extracted for all

compositions (**Figure 5**a). Apart from an increase in E_B contributing to an increase in U_r, the decrease in U_{loss} (area enclosed within the polarization-electric field hysteresis loop) also played a significant role in the enhancement of the overall efficiency of the solid solutions. As seen in the trend for E_B, $Pb_{0.5}Sr_{0.5}HfO_3$ was found to exhibit the best energy-storage performance with a U_r = 77 ± 5 J/cm^3 and η = 97 ± 2%. This corresponds to a 2.7-times increase in U_r from 21 J/cm^3 in $PbHfO_3$ with a remarkable η. Another important aspect for capacitive-energy storage is the need for significant electric fatigue resistance and thermal endurance, with both being essential for maintaining the physical and operational integrity of the devices over a long period of use. The fatigue of two compositions (x = 0 and 0.5) was measured by repeatedly cycling the devices and measuring the polarization-electric field hysteresis loops as a function of the number of cycles at E_{max} = 1.23, 3, and 5.12 MV/cm (Experimental Section). The $PbHfO_3$ heterostructures were found to break down after ~900 cycles (Figure S16a, Supporting Information) at E_B = 1.23 MV/cm, whereas, the $Pb_{0.5}Sr_{0.5}HfO_3$ heterostructures did not show any cyclic fatigue even after 10^9 cycles (a 10^6-times improvement in fatigue endurance). Furthermore, while the $PbHfO_3$ heterostructures could not sustain any fatigue measurements at E_{max} = 3 and 5.12 MV/cm, the $Pb_{0.5}Sr_{0.5}HfO_3$ heterostructures sustained $3x10^5$ and $7x10^4$ cycles, respectively (Figure S17a-c, Supporting Information). The U_r and η values for $PbHfO_3$ and $Pb_{0.5}Sr_{0.5}HfO_3$ as a function of number of cycles are summarized (Figure 5b) wherein the $Pb_{0.5}Sr_{0.5}HfO_3$ heterostructures exhibit no significant degradation in terms of their capacitive-energy-storage performance. Additionally, the thermal endurance of the $PbHfO_3$ and $Pb_{0.5}Sr_{0.5}HfO_3$ heterostructures was tested by performing polarization-electric field hysteresis loop measurements up to their respective E_B

values as a function of temperature (298-573 K) (Figures S16b and S17d, Supporting Information). Though the U_r and η values degraded at higher temperatures in both compositions, the percentage change in U_r was lower in $Pb_{0.5}Sr_{0.5}HfO_3$ (6.5%) as compared to that in $PbHfO_3$ (15.9%) making it a better candidate for capacitive-energy storage (Figure 5c). This claim is further supported by the fact that the U_r and η values for the $Pb_{0.5}Sr_{0.5}HfO_3$ films are on par with (or better than) those of all antiferroelectric materials reported in the literature (Figure 5d[9,29,31,57-69]). All studies on (chemically modified) antiferroelectric thin films for capacitive-energy-storage applications have focused on three material systems: $PbZrO_3$, $(Pb_{1-x}La_x)(Zr_{1-y-z}Ti_yNb_z)O_3$, and HfO_2[56]. To the best of our knowledge, there have been no studies on the energy-storage behavior of $Pb_{1-x}Sr_xHfO_3$ single-crystalline films. A literature review (Figure 5d) shows that obtaining high U_r and η values concomitantly in antiferroelectric materials is immensely challenging. In the current work, however, we have successfully obtained a significantly high U_r (77 ± 5 J/cm^3) along with an unusually high η (97 ± 2%) by virtue of the reduction of hysteresis loss and enhancement of E_B by chemically modifying the antiferroelectric $PbHfO_3$, thus providing tremendous potential for implementation in real-life device applications.

Conclusion

Here, we showed that it is possible to synthesize high-quality epitaxial thin films of orthorhombic (240_o)-oriented $PbHfO_3$ and cubic (001)-oriented $SrHfO_3$ on $SrTiO_3$ (001) (and other) substrates. This was followed by structural, dielectric, and electrical characterization of the as-grown heterostructures. While $PbHfO_3$ films demonstrated robust antiferroelectric

properties, $SrHfO_3$ heterostructures did not exhibit ferroelectric behavior across the temperature range (77-623 K) studied nor under applied electric fields (-3 MV/cm to 3 MV/cm). The lack of a long-range polar order in $SrHfO_3$ was contextualized by first-principles studies that found that there is only a small energy change within the accuracy of our calculations (ΔE = 0.62 meV/atom) associated with the structural distortion from the non-polar ($Pm\bar{3}m$) to the polar ($P4mm$) phase. Additionally, we evaluated the synthesis and capacitive-energy-storage performance of $Pb_{1-x}Sr_xHfO_3$ (x = 0, 0.05, 0.15, 0.25, 0.5, 0.75, 1) thin-film heterostructures on $SrTiO_3$ (001) substrates. It was observed that increasing the strontium content leads to an increase in E_B as well as a decrease in U_{loss} resulting in considerable enhancement of U_r and η at optimum compositions ($Pb_{0.5}Sr_{0.5}HfO_3$). This optimized material provided strong all-around performance as a potential candidate for capacitive-energy-storage applications, with E_B = 5.12 ± 0.5 MV/cm, U_r = 77 ± 5 J/cm^3, and η = 97 ± 2%, accompanied by fatigue endurance and thermal stability comparable to that of the best known antiferroelectric and/or paraelectric oxides reported in the literature.

Experimental Section

Growth of thin-film heterostructures. All thin-film heterostructures were grown using pulsed-laser deposition in an on-axis geometry with a target-to-substrate distance of 55 mm, using a KrF excimer laser (248 nm, LPX 300, Coherent). All thin-film heterostructures with compositions of $PbHfO_3$ and $SrHfO_3$ were grown from ceramic targets with 45-50-nm-thick $SrRuO_3$ layers as the top and bottom electrodes. Multiple targets were tested for the growth of the $PbHfO_3$ thin films (*i.e.*, $PbHfO_3$, $Pb_{1.1}HfO_3$, $Pb_{1.2}HfO_3$) in order to account for the

potentially volatile nature of lead. In the end, stoichiometric $PbHfO_3$ films can be obtained from the different target compositions by carefully controlling various growth parameters. For $PbHfO_3$, 15-360-nm-thick films were deposited on multiple substrates [*i.e.*, $SrTiO_3$ (001), $TbScO_3$ (110), and MgO (001)], at heater temperatures from 600-650°C, across a range of dynamic oxygen-partial pressures (10-100 mTorr), laser fluence values (1.4-2 J/cm^2), and at a laser repetition rate of 10 Hz. The oxygen-partial pressure was maintained at a constant value in this range by striking a balance between the flow rate of oxygen into the chamber and the rate at which the oxygen was being pumped out of the chamber. The $SrHfO_3$ thin films were grown from targets with the same nominal composition. For $SrHfO_3$, 30-400-nm-thick films were deposited on multiple substrates [*i.e.*, $SrTiO_3$ (001), $SrTiO_3$ (110), and $NdScO_3$ (110)] at a range of heater temperatures (600-850°C), across various dynamic oxygen-partial pressures (1-100 mTorr), laser fluence values (0.75-2.5 J/cm^2), and laser repetition rates (1-20 Hz). The composition of the $Pb_{1-x}Sr_xHfO_3$ thin-film heterostructures was varied across $0 < x < 1$ through sub-unit-cell-level mixing using two ceramic targets with composition $PbHfO_3$ and $SrHfO_3$ via a programmable target rotator (Neocera, LLC) that was synced with the excimer laser. The growth of the 75-nm-thick $Pb_{1-x}Sr_xHfO_3$ ($0 < x < 1$) films was done on $SrTiO_3$ (001) substrates at a heater temperature of 600°C, a dynamic oxygen pressure of 10 mTorr, a laser fluence of 1.93 J/cm^2, and a laser repetition rate of 10 Hz. In all growths for $PbHfO_3$, $SrHfO_3$, and $Pb_{1-x}Sr_xHfO_3$ ($0 < x < 1$), the heterostructures were cooled from the growth temperature to room temperature at 10°C/min in a static oxygen pressure of ~760 Torr.

Chemical analysis. To determine the stoichiometry of the $PbHfO_3$ films grown across a range of dynamic oxygen-partial pressures (10-100 mTorr), Rutherford backscattering

spectrometry (RBS) was performed on the $PbHfO_3$ films grown on Al_2O_3 (0001) (sapphire) substrates using a National Electrostatics Corp. Model 5SDH pelletron tandem accelerator. This involved a beam of monoenergetic (3.040 MV) and collimated alpha particles (^{4}He nuclei) being made incident on the film surface at an incident angle $\alpha = 22.5°$, exit angle $\beta = 25.35°$, and with a scattering angle $\theta = 168°$. The spectrum was fitted using the software SIMNRA to obtain the molar ratio of the lead and hafnium for $PbHfO_3$.

Determination of crystal structure via X-ray diffraction. The crystal structure of the synthesized epitaxial films was determined using X-ray diffraction studies performed using a high-resolution X-ray diffractometer (Panalytical, X'Pert^3 MRD) with fixed-slit, 1/2° and 1/16° incident optics, copper K_α radiation (1.54 Å), and a receiving slit of 0.275 mm for the PIXcel3D-Medipix3 detector. θ-2θ line scans were performed in order to probe the structure in the direction perpendicular to the plane of the substrate and X-ray rocking curves were completed about the $Pb_{1-x}Sr_xHfO_3$ ($0 \leq x < 1$) 240_o - and $SrHfO_3$ 002-diffraction conditions for the different substrates to assess the crystalline quality of the heterostructures. Asymmetric azimuthal scans were carried out about the $PbHfO_3$ 362_O-, $SrHfO_3$ 103-, $SrHfO_3$ 101-, and $SrTiO_3$ 103-diffraction conditions varying the angle at a fixed 2θ value. Additionally, in order to determine the crystal structure and the lattice parameters of the heterostructures with composition $Pb_{1-x}Sr_xHfO_3$ ($0 \leq x \leq 1$), X-ray diffraction RSM studies were performed about the 362_O-, 084_O-, 240_O-diffraction conditions of the films and 103-diffraction condition of the substrate.

Electrical and dielectric characterization. The electrical properties for all the heterostructures of all compositions [$Pb_{1-x}Sr_xHfO_3$ ($0 \leq x \leq 1$)] were studied for films grown

on $SrTiO_3$ (001) substrates wherein 45-50-nm-thick $SrRuO_3$ films served as both top and bottom electrodes. The measurements were performed with circular-capacitor (diameter 25 and 50 μm) structures patterned on the top electrode using wet chemical etching via 0.1M $NaIO_4$ solution. The polarization as a function of electric field (-10 to 10 MV/cm) for these circular capacitor structures was measured using a Precision Multiferroic Tester (Radiant Technologies, Inc.) as a function of temperature (77-673 K). Dielectric and loss tangent measurements were performed using an E4990A Impedance Analyzer (Keysight Technologies) as a function of temperature (77-673 K) and frequency (1-1000 kHz) up to an AC field strength value of 275 kV/cm. The fatigue behavior was probed via pulsed measurements using a triangular waveform as the excitation pulse applied at a frequency 10 kHz up to 10^9 cycles.

First-principles calculations. Density functional theory calculations were performed using the projector augmented wave (PAW) formalism as implemented within VASP[70]. Within DFT, total energies and structural parameters can be very sensitive to convergence thresholds and the choice of exchange-correlation functional. While Perdew-Burke-Ernzerhof (PBE) gradient-corrected functionals are considered reliable for a wide-range of material systems, these functionals can be subject to "super-tetragonality" errors in certain ferroelectrics and can overestimate both lattice distortions and spontaneous polarizations[71,72]. Therefore, the referenced high-throughput workflow[47] was run separately with the local-density approximation (LDA) and PBE functionals. In both cases, the 5*p*, 6*s*, and 5*d* electrons of the hafnium cations were treated explicitly as valence, as were the 4*s*, 4*p*, and 5*s* electrons in strontium cations and the 2*s* and 2*p* electrons in oxygen anion. We used a plane-wave

energy cutoff of 740 eV and Brillouin-zone integrations were performed with the tetrahedron method with Blöchl corrections[73], using a 9×9×9 Gamma-centered k-point grid. Our calculations were scalar relativistic, but spin-orbit coupling was neglected. The initial $SrHfO_3$ crystal structure atomic coordinates for the $Pm\bar{3}m$ and $P4mm$ phases were obtained from the *Materials Project* database and then fully relaxed until all forces were smaller than 10^{-5} eV/Å (Supporting Information). To calculate the polarization, we followed the procedure implemented in *pymatgen*'s analysis ferroelectricity module, which is described in detail in the referenced high-throughput workflow[47]. We chose interpolation paths containing ten structures and computed the spontaneous polarization using the Berry-phase approach, following the module's documentation.

Acknowledgements

This work was primarily supported by the U.S. Department of Energy, Office of Science, Office of Basic Energy Sciences, Materials Sciences and Engineering Division under Contract No. DE-AC02-05-CH11231 (Materials Project program KC23MP) for the discovery of novel functional materials. Computational resources used at the Molecular Foundry were supported by the U.S. Department of Energy, Office of Science, Office of Basic Energy Sciences under contract no. DE-AC02-05CH11231. Additional computational resources were provided by NERSC. E.B. acknowledges support from the National Science Foundation Graduate Research Fellowship under Grant No. 1752814. M.R. acknowledges support from the National Science Foundation under Grant DMR-1708615. Y.J. acknowledges support from the Army Research Office under Grant W911NF-21-1-0126. A.F. acknowledges

support from the Army Research Office under Grant W911NF-21-1-0118. A.D. acknowledges support from the Army Research Office under the ETHOS MURI via cooperative agreement W911NF-21-2-0162. B.H. acknowledges support from the Army Research Laboratory/Army Research Office via the Collaborative for Hierarchical Agile and Resonant Materials (CHARM) under cooperative agreement W911NF-19-2-0119.

Figures and captions:

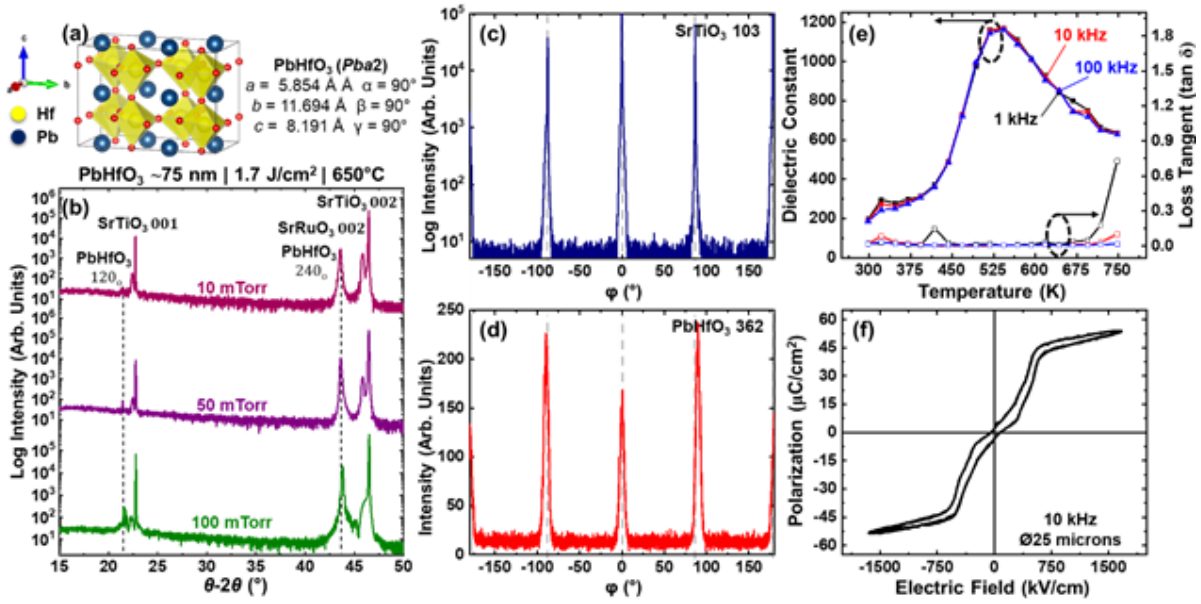

Figure 1. Structural, dielectric, and antiferroelectric properties of epitaxial $PbHfO_3$ thin films. (a) Crystal structure and lattice parameters for orthorhombic antiferroelectric phase of $PbHfO_3$ (*Pba*2). (b) X-ray-diffraction measurement (wide-angle θ-2θ line scan) for 75-nm-thick (240_O)-oriented $PbHfO_3$ films on $SrTiO_3$ (001) substrates as a function of dynamic oxygen-partial pressure during growth (top to bottom, growth at 10, 50, and 100 mTorr) with a fixed heater temperature (650°C) and laser fluence (1.7 J/cm^2). Azimuthal ϕ scans about the (c) $SrTiO_3$ 103-diffraction condition and the (d) $PbHfO_3$ 362_O-diffraction condition. (e) Temperature-dependent dielectric constant (left axis) and loss tangent (right axis) measurements from 298 to 750 K at 1 kHz, 10 kHz, and 100 kHz. (f) Polarization vs. electric field hysteresis loops at room temperature at a frequency of 10 kHz for capacitors 25 microns

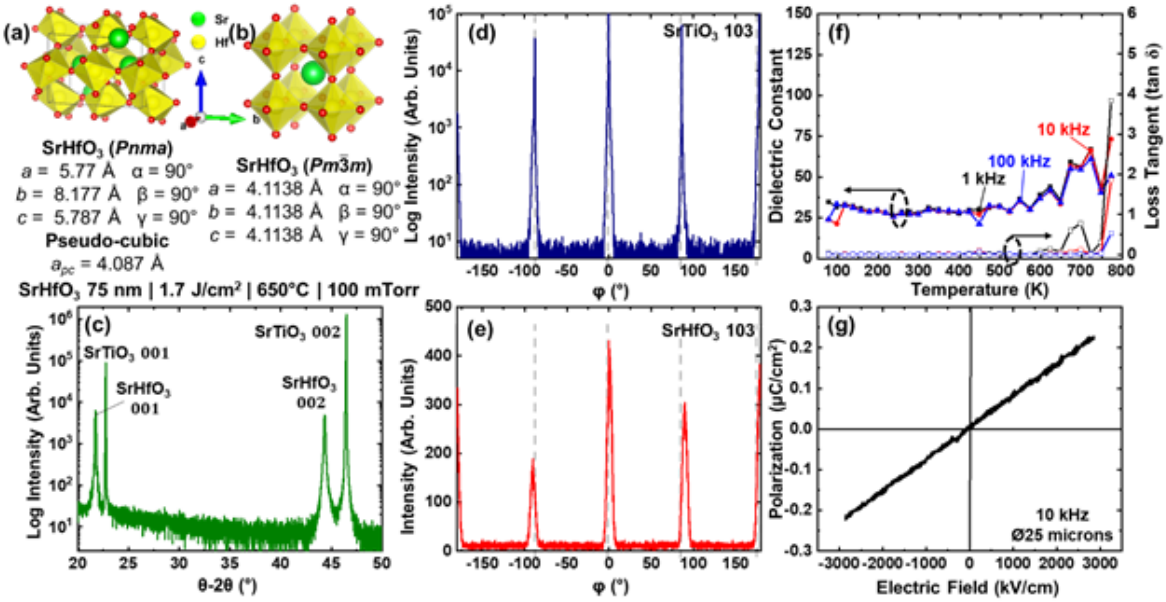

Figure 2. Structural, dielectric, and polarization response of epitaxial $SrHfO_3$ thin films. Crystal structure and lattice parameters for (a) orthorhombic (*Pnma*) and (b) cubic ($Pm\bar{3}m$) phases. (c) X-ray diffraction measurement (wide-angle θ-2θ line scan) for 75-nm-thick (001)-oriented $SrHfO_3$ on a $SrTiO_3$ (001) substrate grown at a heater temperature (650°C), laser fluence (1.7 J/cm^2), and at dynamic oxygen partial pressure 100 mTorr during growth. Azimuthal scans about the (d) $SrTiO_3$ 103-diffraction condition and (e) $SrHfO_3$103-diffraction condition. (f) Temperature-dependent dielectric constant (left axis) and loss tangent (right axis) measurements from 77 to 750 K at 1 kHz, 10 kHz, and 100 kHz. (g) Polarization vs. electric field hysteresis loops at room temperature at a frequency of 10 kHz for capacitors 25 microns in diameter.

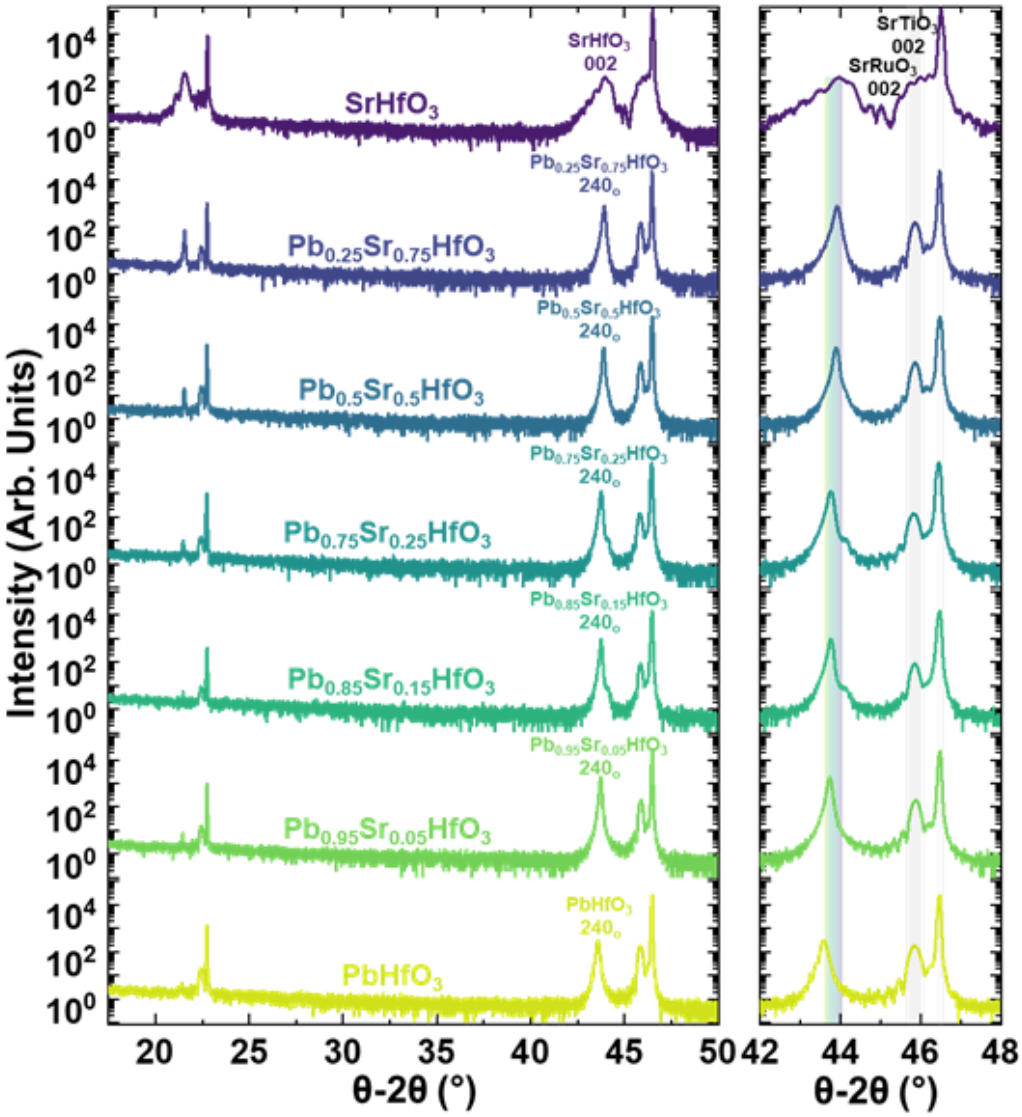

Figure 3. X-ray diffraction measurement (wide-angle θ-2θ line scan, left) for 75-nm-thick epitaxial (240_O)-oriented $Pb_{1-x}Sr_xHfO_3$ (x = 0, 0.05, 0.15, 0.25, 0.5, 0.75, 1) thin films on $SrTiO_3$ (001) substrates grown at a heater temperature (600°C), laser fluence (1.7 J/cm^2), and at dynamic oxygen partial pressure 10 mTorr. A zoom-in about the 240_O-diffraction condition for $Pb_{1-x}Sr_xHfO_3$ (right) includes a peak corresponding to the 002_{pc}-diffraction condition for $SrRuO_3$.

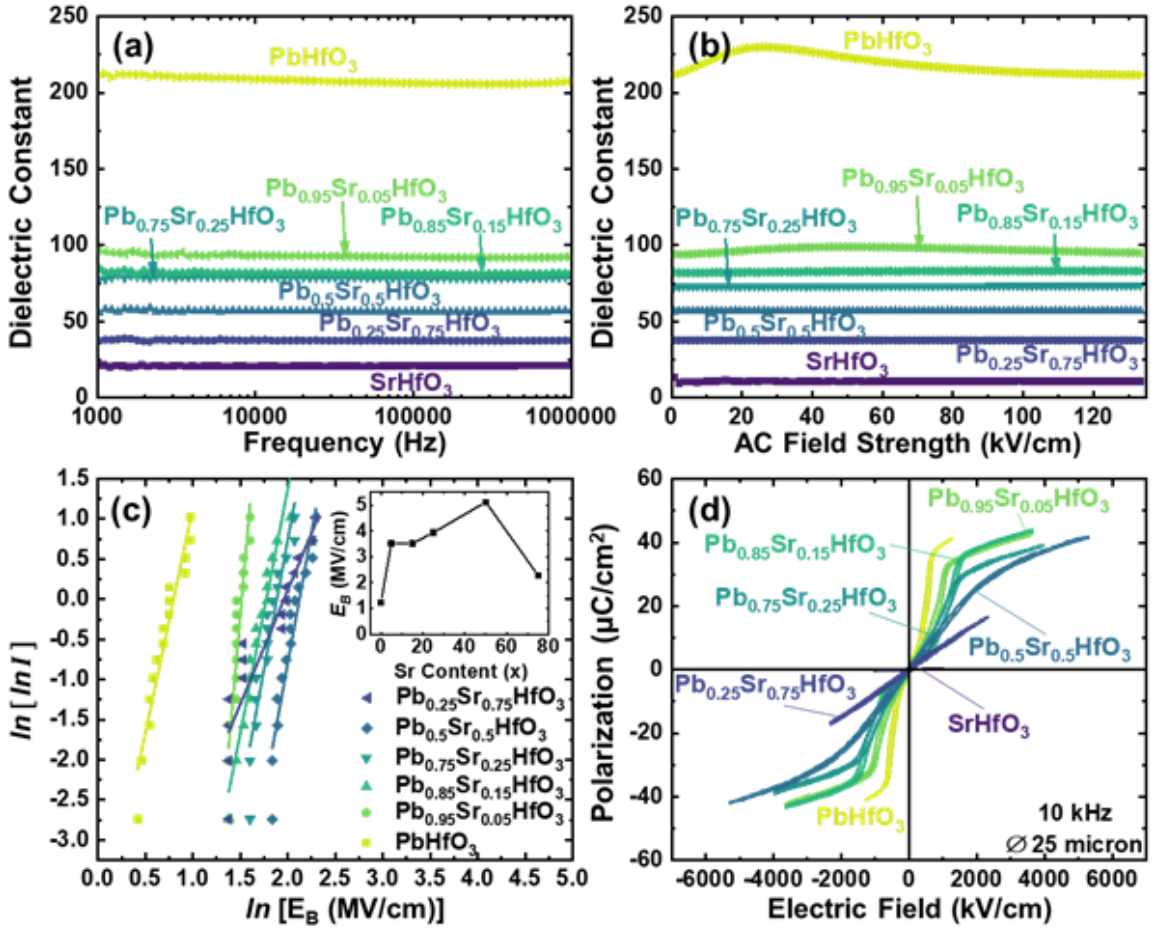

Figure 4. Dielectric and polarization response of 75-nm-thick epitaxial (240_O)-oriented $Pb_{1-x}Sr_xHfO_3$ (x = 0, 0.05, 0.15, 0.25, 0.5, 0.75, 1) thin films on $SrTiO_3$ (001) substrates. Dielectric constant measurements as a function of (a) frequency from 1 kHz to 1000 kHz and (b) applied AC electric field up to 133 kV/cm at a frequency of 10 kHz. (c) Weibull analysis for determination of electric-breakdown strength (E_B) where I on the y-axis represents $\frac{1}{1-\frac{1}{16}}$; inset shows the variation in E_B as a function of strontium content in $Pb_{1-x}Sr_xHfO_3$ solid solution compositions. (d) Polarization vs. electric field hysteresis loop measurements as a frequency of 10 kHz with capacitors 25 microns in diameter driven up to their respective E_B

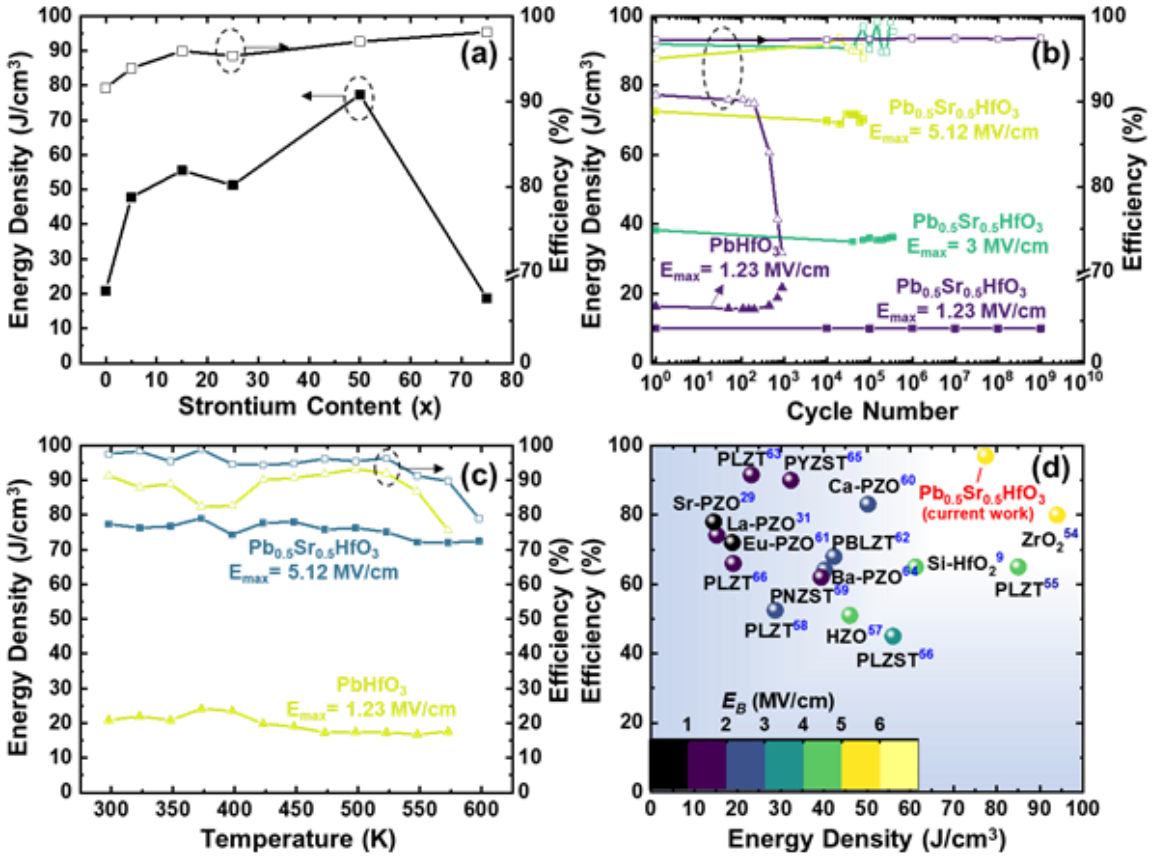

Figure 5. Energy-storage performance for 75-nm-thick epitaxial (240_O)-oriented $Pb_{1-x}Sr_xHfO_3$ ($x = 0$, 0.05, 0.15, 0.25, 0.5, 0.75, 1) thin films on $SrTiO_3$ (001) substrates. (a) Plot of energy density (left-axis) and efficiency (right-axis) as a function of strontium content (x). (b) Cyclic fatigue at a frequency of 10 kHz at electric field values of 1.23 MV/cm, 3 MV/cm, and 5.12 MV/cm for $Pb_{0.5}Sr_{0.5}HfO_3$ and 1.23 MV/cm for $PbHfO_3$. (c) Temperature (298-573 K) evolution of the energy storage density at the corresponding E_B values for $PbHfO_3$ and $Pb_{0.5}Sr_{0.5}HfO_3$ compositions. (d) Summary of energy density and efficiency values for antiferroelectric materials reported in the recent past.

Exploring the $Pb_{1-x}Sr_xHfO_3$ System and Potential for High Capacitive Energy Storage Density and Efficiency

Megha Acharya[1,2], Ella Banyas[2], Maya Ramesh[1], Yizhe Jiang[1], Abel Fernandez[1], Arvind Dasgupta[1], Handong Ling[1], Brendan Hanrahan,[3] Kristin Persson[1,2,4], Jeffrey B. Neaton[2,4,5,6], Lane W. Martin[1,2*]

[1] Department of Materials Science and Engineering, University of California, Berkeley, Berkeley, CA 94720, USA

[2] Materials Sciences Division, Lawrence Berkeley National Laboratory, Berkeley, CA 94720, USA

[3] U.S. Army Research Laboratory, Adelphi, MD 20783, USA

[4] Molecular Foundry, Lawrence Berkeley National Laboratory, Berkeley, CA 94720, USA

[5] Department of Physics, University of California, Berkeley, Berkeley, CA 94720, USA

[6] Kavli Energy Nanosciences Institute, University of California, Berkeley, CA 94720, USA

Table of Contents

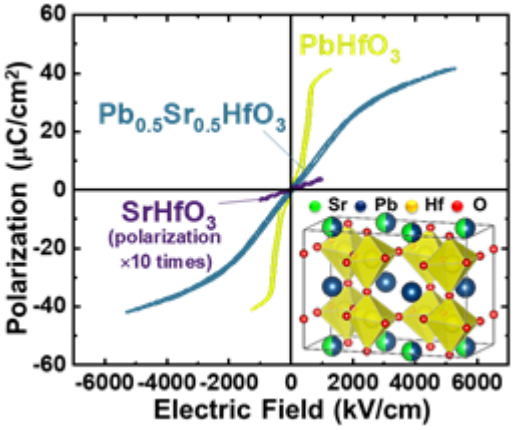

The structural and electrical properties of antiferroelectric $PbHfO_3$ and 'potentially' ferroelectric $SrHfO_3$ are explored. Further, the energy-storage properties of the solid solution $Pb_{1-x}Sr_xHfO_3$ ($0 \leq x < 1$) films are probed. An optimum strontium content is identified that leads to increased electric-breakdown strength and decreased hysteresis-loss in $PbHfO_3$ resulting in concurrent enhancement of the capacitive energy storage density and efficiency.

References

1 K. Black, M. Werner, R. Rowlands-Jones, P. R. Chalker, M. J. Rosseinsky, *Chem. Mater.* **2011**, 23, 2518–2520.

2 S. Migita, Y. Morita, M. Masahara, H. Ota, *Jpn. J. Appl. Phys.* **2014**, 53, 04EA03.

3 J. Müller, T.S. Böscke, S. Müller, E. Yurchuk, P. Polakowski, J. Paul, D. Martin, T. Schenk, K. Khullar, A. Kersch, W. Weinreich, S. Riedel, K. Seidel, A. Kumar, T.M. Arruda, S.V. Kalinin, T. Schlösser, R. Boschke, R. van Bentum, U. Schröder, T. Mikolajick. 2013 IEEE International Electron Devices Meeting, **2013**, 10.8.1-10.8.4.

4 M. H. Park, Y. H. Lee, T. Mikolajick, U. Schroeder, C. S. Hwang, *MRS Communications.* **2018**, 8, 795–808.

5 Z. Lu, W. Bao, G. Wang, S. Sun, L. Li, J. Li, H. Yang, H. Ji, A. Feteira, D. Li, F. Xu, A. K. Kleppe, D. Wang, S. Liuh, I. M. Reaney. *Nano Energy* **2021**, 79, 105423.

6 T. Zhang, Y. Zhao, W. Li, W. Fei. *Energy Storage Materials* **2019**, 18, 238–245.

7 M.D. Nguyen, E. P. Houwman, M. T. Do, G. Rijnders. *Energy Storage Materials* **2020**, 25, 193–201.

8 W. Chao, T. Yang, Y. Li. *J. Mater. Chem. C* **2020** 8 17016.

[9] F. Ali, X. Liu, D. Zhou, X. Yang, J. Xu, T. Schenk, J. Muller, U. Schroeder, F. Cao, X. Dong. *J. Appl. Phys.* **2017** 122, 144105.

[10] M. G. Kozodaev, A. G. Chernikova, R. R. Khakimov, M. H. Park, A. M. Markeev, C. S. Hwang. *Appl. Phys. Lett.* **2018**, 113, 123902.

[11] M. H. Park, H. J. Kim, Y. J. Kim, T. Moon, K. D. Kim, C. S. Hwang. *Nano Energy* **2015**, 12, 131–140.

[12] G. Shirane, *Phys. Rev.* **1952**, 86, 219–227.

[13] M. F. Kuprianov, S. M. Zaitsev, E. S. Gagarina, E. G. Fesenko. *Phase Transitions* **1983**, 4, 55–63 (1983).

[14] D. L. Corker, A. M. Glazer, W. Kaminsky, R. W. Whatmore, J. Dec and K. Roleder. *Acta Crystallogr. Sect. B Struct. Sci.* **1998**, 54, 18–28.

[15] S. Huband, A. M. Glazer, K. Roleder, A. Majchrowski, P. A. Thomas. *J. Appl. Crystallogr.* **2017**, 50, 378–384.

[16] K. Roleder, M. Maglione, M. D. Fontana, I. Jankowska-Sumara, G. E. Kugel, J. Dec. *Ferroelectrics* **2000**, 238, 139–146.

[17] F. Jona, G. Shirane, F. Mazzi, R. Pepinsky. *Phys. Rev.* **1957**, 105, 849-856.

[18] O. I. Prokopalo, I. P. Raevskii, M. A. Malitskaya, Y. M. Popov, A. A. Bokov, V. G. Smotrakov. *Ferroelectrics* **1982**, 45, 89-95.

[19] X. Huang, T. Zhang, W. Wang, P. Ge, X. Tang. *Materials and Design* **2021** 204, 109666.

[20] B. Hanrahan, C. Milesi-Brault, A. Leff, A. Payne, S. Liu, M. Guennou, N. Strnad. *APL Mater.* **2021**, 9, 021108.

[21] X. Huang, T. Zhang, R. Gao, H. Huang, P. Ge, H. Tang, X. Tang. *ACS Appl. Mater. Interfaces* **2021**, 13, 21331−21337.

[22] B. J. Kennedy, C. J. Howard, B. C. Chakoumakos. *Phys. Rev. B - Condens. Matter Mater. Phys.* **1999**, 60, 2972–2975.

[23] M. K. Singh, G. Singh, T. H. Kim, S. Kojima, R. S. Katiyar, J. F. Scott. *EPL* **2014**, 107, 26004.

[24] M. Sousa, C. Rossel, C. Marchiori, H. Siegwart, D. Caimi, J. P. Locquet, D. J. Webb, R. Germann, J. Fompeyrine *J. Appl. Phys.* **2007**, 102, 104103.

[25] M. Karmaoui, E. V. Raman, D. M. Tobaldi, L. Lajaunie, M. P. Graça, R. Arenal, M. P. Seabra, J. A. Labrincha, R. C. Pullar. *RSC Adv.* **2016**, 6, 51493–51502.

[26] H. Murata, T. Yamamoto, H. Moriwake, I. Tanaka. *Phys. Status Solidi B* **2009**, 246, 1628–1633.

[27] L. M. Garten, S. Dwaraknath, J. Walker, J. S. Mangum, P. F. Ndione, Y. Park, D. A. Beaton, V. Gopalan, B. P. Gorman, L. T. Schelhas, M. F. Toney, S. Trolier-McKinstry, K. A. Persson, D. S. Ginley. *Adv. Mater.* **2018**, 30, 1800559.

[28] H. Ling, S. S. Dwaraknath, K. A. Persson. *Chem. Mater.* **2020**, 32, 2836–2842.

[29] X. Hao, J. Zhai, X. Yao. *J. Am. Ceram. Soc.* **2009**, 92 1133–1135.

[30] J. D. Jackson. Classical Electrodynamics. New York: Wiley (1998).

[31] H. J. Lee, S. S. Won, K. H. Cho, C. K. Han, N. Mostovych, A. I. Kingon, S. Kim, H. Y. Lee. *Applied Physics Letters* **2018**, 112, 092901.

[32] Y. Z. Li, J. L. Lin, Y. Bai, Y. Li, Z. D. Zhang, Z. J. Wang. *ACS Nano* **2020**, 14, 6857−6865.
[33] J. Parui, S. B. Krupanidhi. *Appl. Phys. Lett.* **2008**, 92, 192901.
[34] K. Singh. *Ferroelectrics* **1989**, 94, 433.
[35] E. Breckenfeld, R. B. Wilson, L. W. Martin. *Appl. Phys. Lett.* **2013**, 103, 082901.
[36] S. K. Sharma, A. Jayaraman, C. P. Chowdhury, S. Y. Wang. *J. Raman Spectrosc.* **1994**, 25, 331-334.
[37] H. Fujishita, Y. Ishikawa. *Ferroelectrics* **2002**, 269**,** 135-140.
[38] O. E. Fesenko, L. E. Balyunis. *Ferroelectrics* **1980**, 29, 95-98.
[39] K. M. Rabe, *Antiferroelectricity in Oxides: A Reexamination. In Functional Metal Oxides* (Eds: S. B. Ogale, T. V. Venkatesan, M. G. Blamire), Wiley-VCH, Weinheim, Germany 2013.
[40] D. Damjanovik. *Rep. Prog. Phys.* **1998**, 61, 1267-1324.
[41] S. Saremi, R. Xu, L. R. Dedon, J. A. Mundy, S. Hsu, Z. Chen, A. R. Damodaran, S. P. Chapman, J. T. Evans, L. W. Martin. *Adv. Mater.* **2016**, 28, 10750–10756.
[42] S. Saremi, R. Xu, L. R. Dedon, R. Gao, A. Ghosh, A. Dasgupta, L. W. Martin, *Adv Mater Interfaces* **2018**, *5*, 1700991.
[43] P. H. Sun, T. Nakamura, Y. J. Shan, Y. Inaguma, M. Itoh. *Ferroelectrics* **1998**, 217, 137-145.
[44] M. Acharya, S. Mack, A. Fernandez, J. Kim, H. Wang, K. Eriguchi, D. Meyers, V. Gopalan, J. Neaton, L. W. Martin. *Chem. Mater.* **2020**, 32, 7274−7283.
[45] M. G. Stachiotti, G. Fabricius, R. Alonso, C. O. Rodriguez. *Phys. Rev. B* **1998**, 58, 8145–8148.
[46] R. Vali. *Solid State Communications* **2008**, 148, 29–31.
[47] T. E. Smidt, S. A. Mack, S. E. Reyes-Lillo, A. Jain & J. B. Neaton. *Sci. Data* **2020**, 7, 72.
[48] Y. Zhang, J. Sun, J. P. Perdew, & X. Wu. *Phys. Rev. B* **2017**, 96, 035143.
[49] M. Sawkar-Mathur, C. Marchiori, J. Fompeyrine, M. F.Toney, J. Bargar, J. P.Chang. *Thin Solid Films* **2010**, 518, 118–122.
[50] M. D. McDaniel, C. Hu, S. Lu, T. Q. Ngo, A. Posadas, A. Jiang, D. J. Smith, E. T. Yu, A. A. Demkov, J. G. Ekerdt. *J. Appl. Phys.* **2015**, 117, 054101.
[51] K. Wu, W. A. Schulze. *J. Am. Ceram. Soc.* **1992**, 75, 3385-3389.
[52] K. Nadaud, C. Borderon, R. Renoud, M. Bah, S. Ginestar, H. W. Gundel. *Appl. Phys. Lett.* **2021**, 118, 042902.
[53] Z. Luo, X. Lou, F. Zhang, Y. Liu, D. Chang, C. Liu, Q. Liu, B. Dkhil, M. Zhang, X. Ren, H. He. *Applied Physics Letters* **2014**, 104, 142904.
[54] M. D. Coulibaly, C. Borderon, R. Renoud, H. W. Gundeld. *Appl. Phys. Lett.* **2020**, 117, 142905.
[55] W. J. Weibull. *Appl. Mech*. **1951**, 73, 293−297.
[56] H. Palneedi, M. Peddigari, G. Hwang, D. Jeong, J. Ryu. *Adv. Funct. Mater.* **2018**, 28, 1803665.
[57] S. Yi, H. Lin, M. Chen. *J. Mater. Chem. A* **2021**, 9, 9081-9091.

[58] B. Ma, Z. Hu, R. E. Koritala, T. H. Lee, S. E. Dorris, U. Balachandran. *J Mater Sci: Mater Electron* **2015**, 26, 9279–9287.
[59] X. Hao, Y. Wang, L. Zhang, L. Zhang, S. An. *Appl. Phys. Lett.* **2013**, 102, 163903.
[60] M. H. Park, H. J. Kim, Y. J. Kim, T. Moon, K. D. Kim, C. S. Hwang. *Adv. Energy Mater.* **2014**, 4, 1400610.
[61] X. Hao, Y. Wang, J. Yang, S. An, J. Xu. *Journal of Applied Physics* **2012**, 112, 114111.
[62] B. Shen, Y. Li, N. Sun, Y. Zhao, X. Hao. *Nanoscale* **2020**, 12, 8958-8968.
[63] Y. Z. Li, Z. J. Wang, Y. Bai, Z. D. Zhang. *Journal of the European Ceramic Society* **2020**, 40, 1285–1292.
[64] M. Ye, Q. Sun, X. Chen, Z. Jiang, F. Wang. *J. Am. Ceram. Soc.* **2011** 94, 3234–3236.
[65] H. Gao, N. Sun, Y. Li, Q. Zhang, X. Hao, L. B. Kong, Q. Wang. *Ceramics International* **2016**, 42, 16439–16447.
[66] M. D. Nguyen, C. T.Q. Nguyen, H. N. Vu, G. Rijnders. *Journal of the European Ceramic Society* **2018**, 38, 95–103.
[67] B. Peng, Q. Zhang, X. Li, T. Sun, H. Fan, S. Ke, M. Ye, Y. Wang, W. Lu, H. Niu, X. Zeng, H. Huang. *ACS Appl. Mater. Interfaces* **2015**, 7, 13512−13517.
[68] C. W. Ahn, G. Amarsanaa, S. S. Won, S. A Chae, D. S. Lee, I. W. Kim. *ACS Appl. Mater. Interfaces* **2015**, 7, 26381−26386.
[69] J. Ge, X. Dong, Y. Chen, F. Cao, G. Wang. *Appl. Phys. Lett.* **2013**, 102, 142905.
[70] P. E. Blöchl, *Phys. Rev. B* **1994** 50, 17953.
[71] Y. Zhang, J. Sun, J. P. Perdew, and X. Wu, *Phys. Rev. B* **2017** 96, 035143.
[72] D. I. Bilc, R. Orlando, R. Shaltaf, G.-M. Rignanese, J. Íñiguez, and P. Ghosez, *Phys. Rev. B* **2008**, 77, 165107.
[73] P. E. Blöchl, O. Jepsen, O. K. Andersen, *Phys. Rev. B* **1994** 49, 16223.